

Article

Study on Debinding and Sintering Processes for Ceramics Fabricated Using Digital Light Processing (DLP) 3D Printing

Jae-Ho Sim ¹, Bon-Keup Koo ², Minhun Jung ^{3,*} and Dong-Soo Kim ^{1,*}

¹ Department of Creative Convergence Engineering, Hanbat National University, Yuseong-ku, Daejeon 305-719, Republic of Korea

² Department of Materials Science and Engineering, Hanbat National University, Yuseng-ku, Daejeon 305-719, Republic of Korea

³ Research Institute of Printed Electronics & 3D Printing, Hanbat National University, Yuseng-ku, Daejeon 305-719, Republic of Korea

* Correspondence: jungminhun@gmail.com (M.J.); kds671@hanbat.ac.kr (D.-S.K.); Tel.: +82-42-821-1734 (M.J.); +82-42-821-1734 (D.-S.K.)

Abstract: Ceramics have excellent properties such as hardness and thermal and chemical stability. Therefore, researchers have studied the use of 3D printing to produce complex shapes in tools and structural applications. The debinding and sintering processes for ceramic composite materials manufactured using digital light processing (DLP) 3D printing technology were studied. The slurry used for DLP 3D printing requires debinding and sintering, as it contains ceramics and binders. Therefore, the debinding and sintering processes were measured by TG-DSC curves, and the changes in material characteristics were evaluated by setting the debinding holding time (4, 5, and 6 h) and sintering temperature (1100, 1200, and 1300 °C) as parameters. After debinding for 6 h, the density of the ceramic sintered at 1300 °C was 1.36 g/cm³; the linear shrinkage was 22.1%/21.6%/28.5% along the x, y, and z axes, respectively; and the bending strength was 8.58 MPa. As a result of this study, we developed an optimized process for the debinding and sintering of ceramics manufactured through the DLP 3D printing process.



Citation: Sim, J.-H.; Koo, B.-K.; Jung, M.; Kim, D.-S. Study on Debinding and Sintering Processes for Ceramics Fabricated Using Digital Light Processing (DLP) 3D Printing. *Processes* **2022**, *10*, 2467. <https://doi.org/10.3390/pr10112467>

Received: 6 September 2022

Accepted: 18 November 2022

Published: 21 November 2022

Publisher's Note: MDPI stays neutral with regard to jurisdictional claims in published maps and institutional affiliations.



Copyright: © 2022 by the authors. Licensee MDPI, Basel, Switzerland. This article is an open access article distributed under the terms and conditions of the Creative Commons Attribution (CC BY) license (<https://creativecommons.org/licenses/by/4.0/>).

1. Introduction

Ceramics have excellent properties, including high mechanical strength and hardness, excellent thermal and chemical stability, as well as high wear resistance. Owing to these excellent properties, ceramics have been applied to a wide range of fields including chemistry, machinery, electronics, aerospace, space, and biotechnology [1–5]. The ceramic component is typically powder and is molded in the form of a suspension containing binder and other additives, which then goes through a high-temperature densification process to obtain the desired physical properties. The conventional ceramic manufacturing process proceeds through a series of operations ranging from powder processing to molding and sintering using expensive dies or molds. However, there are limitations in the conventional ceramic manufacturing process owing to difficulties in producing complex parts that significantly increase manufacturing cost and production time [6–9]. To overcome these process limitations, the 3D printing method was studied.

Among the 3D printing methods, digital light processing (DLP) 3D printing is a curing method that uses a projector to radiate UV light into a vat containing acrylic-based photosensitive resins [1]. Compared with stereolithography (SLA), which employs a laser for curing, the DLP 3D process is relatively fast, as it cures one plane, and is thus suitable for industrial applications [10,11].

The ceramic green body fabricated by 3D printing undergoes heat treatment processes, such as debinding and sintering, to achieve a sintered body with the essential final properties. In the debinding process, the binder present in the ceramic slurry must be removed by

pyrolysis. However, the excessive heating rate, inappropriate holding zone, and holding time generate microcracks as the binder diffuses from the ceramic green body [12]. When microcracks are not removed, the mechanical properties deteriorate as a result of these microcracks during sintering. Therefore, the heating rate and holding zone in a temperature range where the binder decomposes must be determined accurately before providing thermal stabilization of the ceramic green body by means of a suitable holding time [13]. In addition, a suitable sintering temperature is required, as the ceramic densification process is not completely achieved when using an inappropriate heating temperature in the sintering process, causing physical property deterioration.

In this study, an optimal ceramic composite material was fabricated from a green body prepared by DLP 3D printing through heat treatment processes. By applying different holding times in the debinding process and sintering temperatures as parameters, the mechanical properties were systematically studied by measuring the density, dimensional shrinkage, phase composition, microstructure, and bending strength of the ceramic sintered body. Finally, ceramic lattice structures with a complex geometry were fabricated by applying the optimized conditions for the debinding and sintering processes, and the possibility of manufacturing ceramic parts using DLP 3D printing was presented.

2. Experiment

In this study, a ceramic sintered body was manufactured through a series of processes, as shown in Figure 1. We used the instrumentations of the DLP 3D printer (Carima Co. Ltd., Seoul, Republic of Korea), ceramic slurry (Carima Co. Ltd., Seoul, Republic of Korea). A three-dimensional cuboid model was designed using 3D CAD modeling. The size of the sample was 25 mm × 5 mm × 3.17 mm. For the experiment, the thickness and conditions of each layer were set as follows. The initial layer was irradiated with a long exposure time of 80 s up to 10 layers to firmly adhere the model and the substrate, while the normal exposure time was set to 10 s. For post-treatment, the sample was placed in an ethanol solution and washed in an ultrasonic cleaner for 5 min, followed by UV curing for 15 min.

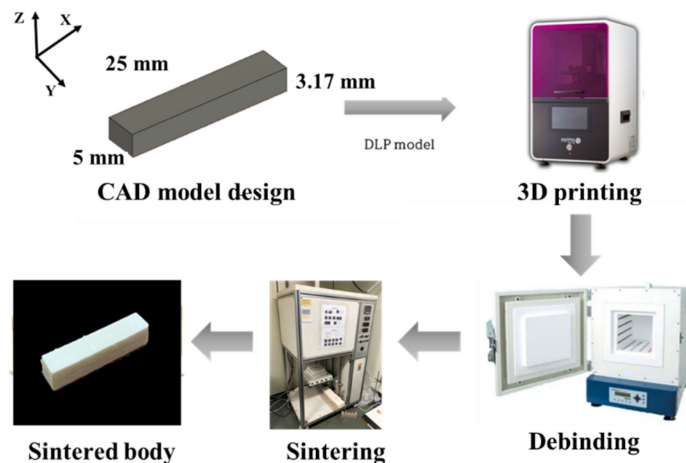


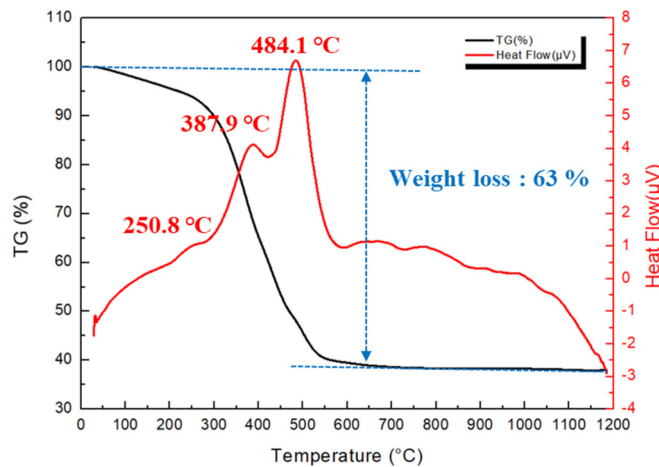
Figure 1. Flow diagram of the ceramic composite material.

Table 1 shows the component ratio of the ceramic slurry. In the debinding process, the binder inside the printed ceramic was pyrolyzed into a gas state by heat treatment, so that only ceramic existed. When a fast-heating rate and inappropriate holding zone were set in this process, gas was generated as the binder was pyrolyzed, resulting in thermal stress. Consequently, pores and cracks were formed in the passages through which the binder inside the ceramic diffused. Thus, the temperature range at which the binder is thermally decomposed must be accurately identified by a TG-DSC curve before the debinding process.

Table 1. Ceramic slurry component ratio.

Ceramic Slurry Component (CCTP17W)	Mass Percentage (wt %)
Al ₂ O ₃	20–40
SiO ₂ (Quartz)	5–15
Kaolin	5–15
Ceramic frit	1–10
Calcium inosilicate	1–10
Borosilicate frit	1–10
Urethane acrylate resin	10–30
Alkox.Pentaerythritol tetracrylate	10–30
Urethane acrylate	5–15
2-Propenoic Acid	<0.1
2,6-di-tert-butyl-p-cresol	0.1–1
Dibutyltin dilaurate	<0.15
2,4,6-Trimethylbenzoyldiphenylphosphine oxide	0.12–2
2,5-thiophenediyldis (5-tert-butyl-1, 3-benzoxazole)	0.001–1
Silica, amorphous, fumed, cryst, -free	0.1–2

The TG-DSC curve of the ceramic green body fabricated by the DLP 3D printer is shown in Figure 2. First, an endothermic reaction gradually increased from 25 °C to 200 °C, as seen in the DSC curve. Then, distinct endothermic peaks were observed at 250.8 °C, 387.9 °C, and 484.1 °C. The main range for thermal decomposition of the binder was found to be 250–485 °C. The TG curve shows that the mass of the sample decreased with the increasing temperature. The mass gradually decreased in the range of 25–300 °C, with the most significant decrease observed between 300 and 550 °C. After that, the mass change rate decreased steadily. It was observed that the mass tended to decrease by approximately 63% compared with that before heat treatment at 600 °C. The loss of mass corresponded to the decomposed photosensitive polymer and binder in the slurry, as confirmed by Fourier transform infrared (FTIR) spectroscopy.

**Figure 2.** The TG-DSC curve of the ceramic green body.

Based on the TG-DSC curve, the parameters for the debinding and sintering processes were determined. When establishing the debinding process, the heating rate must be strictly controlled as the binder has a very high thermal decomposition rate, and a sufficient holding time is required to slow the diffusion rate of the gas generated by pyrolysis of the binder [14]. The debinding and sintering profiles obtained through TG-DSC analysis are shown in Figure 3. We used the instrumentations of the debinding furnace (Wisd Co., Ltd., Incheon, Republic of Korea) and sintering furnace (Ah Jeon Co., Ltd., Namyangju, Republic of Korea). During the debinding process, thermal stress occurred from the ceramic samples. Therefore, many researchers have proceeded with the debinding process at a slow heating

rate. It has been found that the slow heating rate was connected to the densification of the sintering process [15,16].

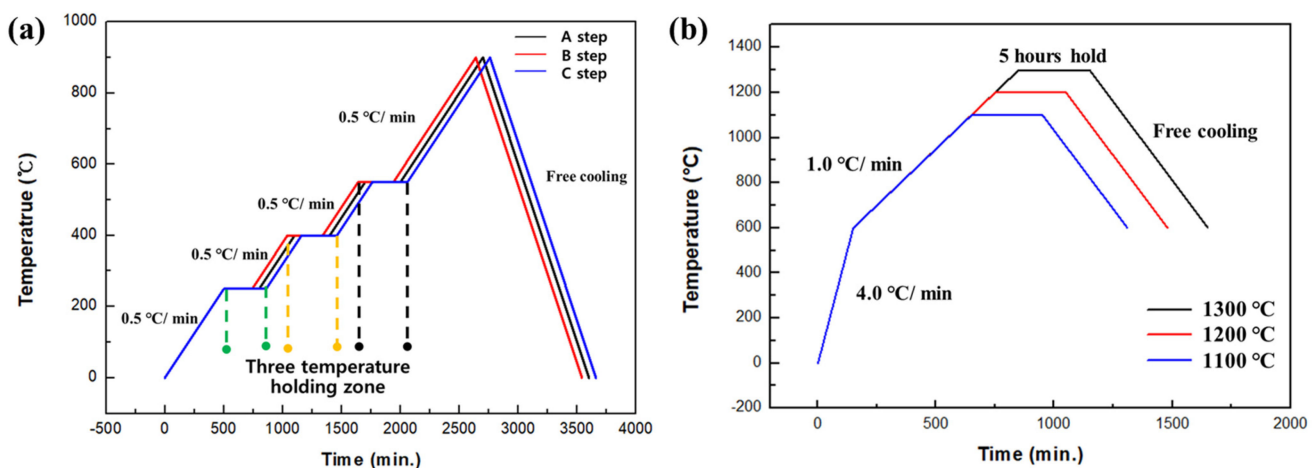


Figure 3. Debinding (a) and sintering (b) profiles. (A step: 4 h, B step: 5 h, C step: 6 h, “step” refers to the three temperature holding zone times).

The heating rate for the debinding process was set to $0.5\text{ }^{\circ}\text{C}/\text{min}$ to minimize thermal stress. The holding times at 250 , 400 , and $550\text{ }^{\circ}\text{C}$ that exhibited distinct endothermic peaks in the DSC curve were 4 , 5 , and 6 h , respectively, and after heating to $900\text{ }^{\circ}\text{C}$ to improve mechanical strength, the sample was cooled naturally. Sintering was carried out by heating to $600\text{ }^{\circ}\text{C}$ at $4.0\text{ }^{\circ}\text{C}/\text{min}$, then proceeding to 1100 , 1200 , and $1300\text{ }^{\circ}\text{C}$ at $1.0\text{ }^{\circ}\text{C}/\text{min}$, with a holding time of 5 h . The sintering temperature plays a major role in the shrinkage and density of ceramics, as it affects the ceramic particle size and the number of pores in the densification process. Thus, the sintering temperature has a significant impact on ceramic properties.

3. Results and Discussion

Figure 4 shows the shrinkage rate of the green body printed by DLP 3D printing, the debinded body (maintained for 6 h), and the sintered body at $1300\text{ }^{\circ}\text{C}$. The sintered body exhibited significant shrinkage owing to the decomposition of photosensitive polymer. Among them, the highest shrinkage rate was observed after debinding, and anisotropic shrinkage was indicated. The anisotropy of shrinkage depends on the actual dimensions of the sample (length–width ratio, length–height ratio, and porosity) [2]. In addition, the uniformity of the ceramic particles plays a key role during layering in the printing process.

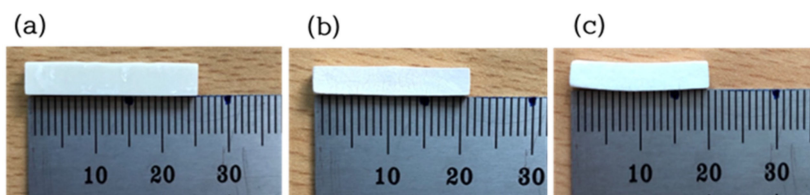


Figure 4. Photographs of the bodies in each stage: (a) green bodies, (b) debinded (6 h holding time) bodies, and (c) sintered bodies at $1300\text{ }^{\circ}\text{C}$.

Table 2 presents the physical properties of the ceramic composite materials according to the sintering temperature, including the weight loss rate after debinding, linear shrinkage rate, and density. The weight loss rate was found to be the same, while the linear shrinkage rate and density increased with a higher sintering temperature. Accordingly, the density of the sample sintered at $1300\text{ }^{\circ}\text{C}$ was 1.36 g/cm^3 , with linear shrinkage rates along the x, y, and z axes of 22.1 , 21.6 , and 28.5% , respectively.

Table 2. Physical properties of the ceramic sample according to the sintering temperature.

Sample	Weight Loss Rate after Debinding (%)	X, Y, and Z Linear Shrinkage (%)	Density (g/cm ³)
1100 °C	60	16.9/20/15.1	1.10
1200 °C	60	20.8/20/21.2	1.14
1300 °C	60	22.1/21.6/28.5	1.36

The chemical structures of the three samples (green body, debinded body, and sintered body) were characterized by the FTIR spectrum. In the case of the green body, the absorption peaks at 996, 1727, and 2880 cm⁻¹ can be attributed to the acrylate groups. After debinding, the acrylate groups' peaks became weaker, indicating that binders were removed after the thermal decomposition. Moreover, the absorption peak at 1064 cm⁻¹ can be assigned to the C-O group of the calcium carbonate (CaCO₃) [17]. In the case of the sintered body, the absorption peaks at 899 and 1146 cm⁻¹ can be attributed to wollastonite and Quartz (SiO₂), respectively [18,19].

The crystallization behavior of the ceramic samples according to sintering temperature and the spectra is shown in Figure 5b. Four kinds of diffraction peaks appeared in the ceramic samples. In the case of the green body, strong diffraction humps were observed, which indicated α -Al₂O₃ at $2\theta = 24.2^\circ, 35.2^\circ, 42.6^\circ, 52.3^\circ, 57.6^\circ, 66.1^\circ, 68.8^\circ$, and 77.4° [20]. Broad diffraction humps were observed at $2\theta = 26.1^\circ, 37.9^\circ, 50.2^\circ$, and 60.1° , which indicated SiO₂ (Quartz) [21]. Strong diffraction humps were observed at $2\theta = 21.7^\circ, 26.9^\circ$, and 29.0° , which were consistent with the characteristic peak (111) of aragonite of CaCO₃ [22]. Additionally, strong diffraction humps were observed at $2\theta = 23.8^\circ, 26.3^\circ$, and 26.6° , indicating β -wollastonite [23]. After being sintered at 1200 °C, diffraction peaks of CaCO₃ were weakened. This was caused by a melting point of about 825 °C in CaCO₃ (aragonite) to change the crystallinity. After being sintered at 1300 °C, peaks were observed at $2\theta = 23.8^\circ, 26.3^\circ$, and 26.6° , which changed the β -wollastonite phase to the α -wollastonite phase [23].

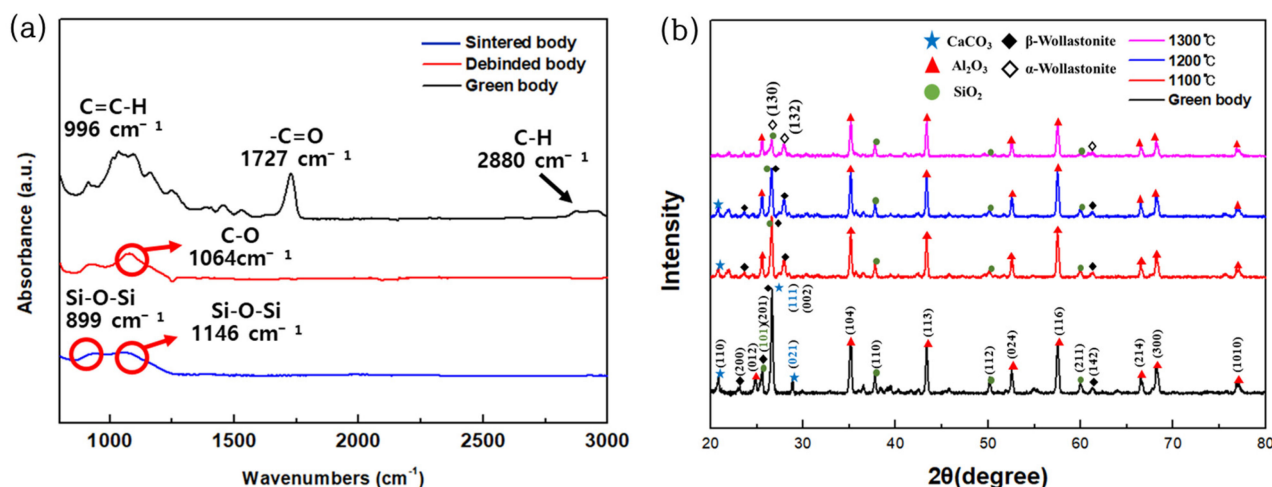


Figure 5. (a) FTIR spectra of the ceramic after pyrolysis at different temperatures, (b) XRD patterns of the ceramic bodies according to different sintering temperatures.

It can be seen that the number of pores gradually decreased with the increasing debinding holding time in Figure 6. Further, it can be seen that the densification gradually formed with the increasing sintering temperature. In conclusion, the SEM images showed that the debinding and sintering processes were optimal when using the C step for debinding and a sintering temperature of 1300 °C. However, the presence of unsintered particles revealed the insufficiency of the sintering temperature. In future research, a study will be conducted for a sintering process at 1600 °C or higher [13].

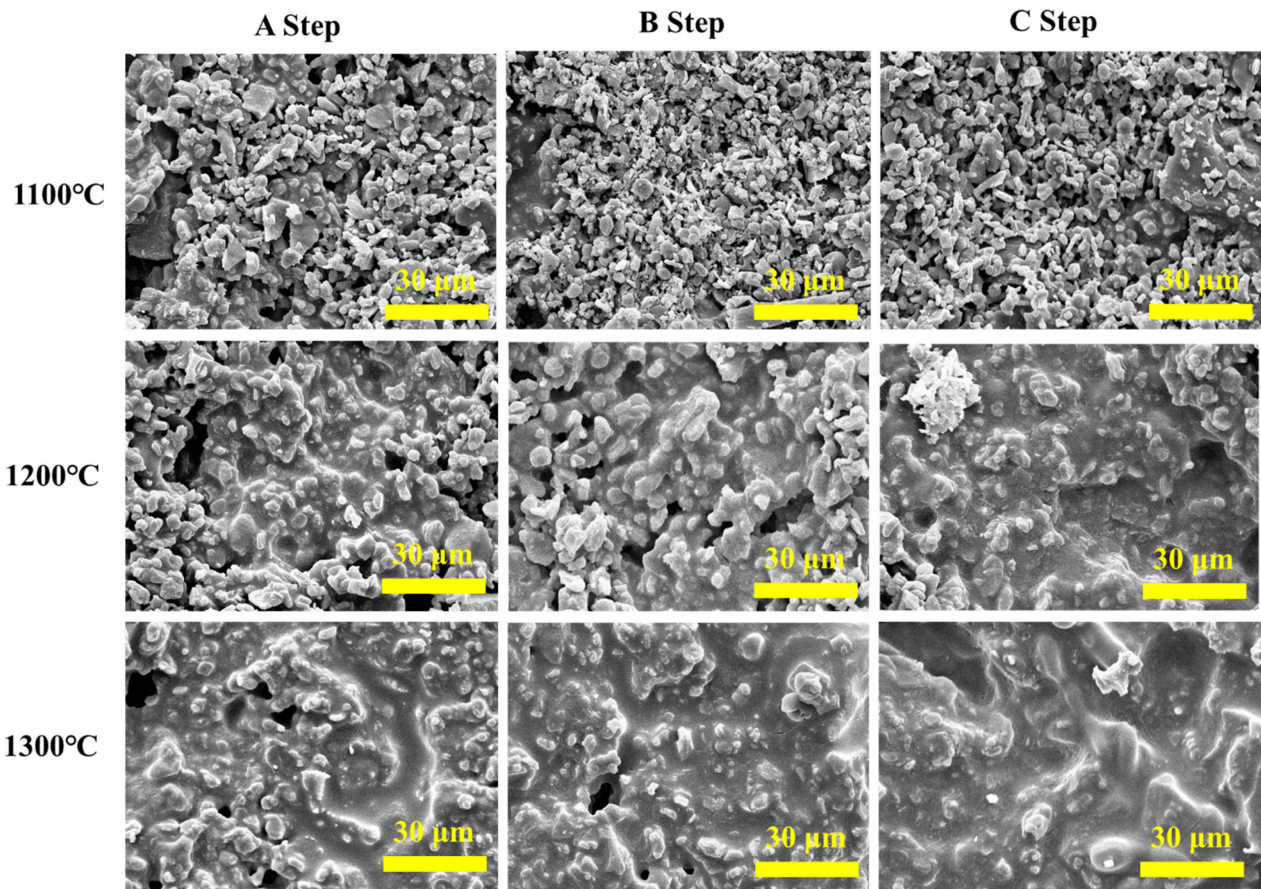


Figure 6. Cross-sectional SEM images of ceramic bodies according to different temperatures with debinding steps A, B, and C.

Figure 7a shows the FE-SEM images and EDAX spectrum of the ceramics on the green body. The particle size of SiO_2 was found to be $5.16 \mu\text{m}$, while that of Al_2O_3 was 675 nm . In the mapping image of the EDAX spectrum, a large amount of carbon was found in the slurry. Figure 8b shows the ceramic sample's SEM image and EDAX spectrum sintered at 1300°C after the C-step debinding process. The particle size of SiO_2 was found to be $4.25 \mu\text{m}$, while that of Al_2O_3 was 837 nm . It could be seen that a few C elements appeared in the sintered particles, which demonstrated that CaSiO_3 contained carbon.

After debinding with the A, B, and C steps, the mechanical properties were determined with respect to sintering temperature by a bending strength test, and the results are shown in Figure 8. Bending strength was measured perpendicular to the x-y plane of the sample. The bending strength of the samples varied from 3.05 to 8.58 MPa . As the holding time of debinding and the temperature of sintering increased, the bending strength gradually increased. The bending strength of the sample sintered at 1300°C reached a maximum value of 8.58 MPa after C-step debinding. However, the bending strength of the Al_2O_3 ceramic, which was fabricated by the existing DLP 3D printer and sintered at 1300°C , exhibited a value of approximately 20 MPa [24]. However, the cutting tool applications of ceramics required a minimum bending strength of approximately 350 MPa [25].

The relatively low bending strength value despite the same sintering temperature can be explained by the ceramic content in the ceramic slurry. With a lower ceramic content, the amount of binder pyrolyzed during debinding was relatively large, thus the size and number of pores increased. Porosity demonstrated that the mechanical properties decreased with the increasing pores [26]. During debinding, the decomposition of binders brings about the formation of defects such as cracks and delaminations. To overcome this issue, researchers studied the inner body with a porous architecture [27]. When the sintering

process was finally performed, it was relatively difficult to densify the ceramic particles. The ceramic slurry in this study had a low ceramic content of 40 wt%, so the number of pores inside the ceramic might be relatively large after debinding and sintering. As a result, the densification process during sintering was not actively performed, which explains why the strength might be low.

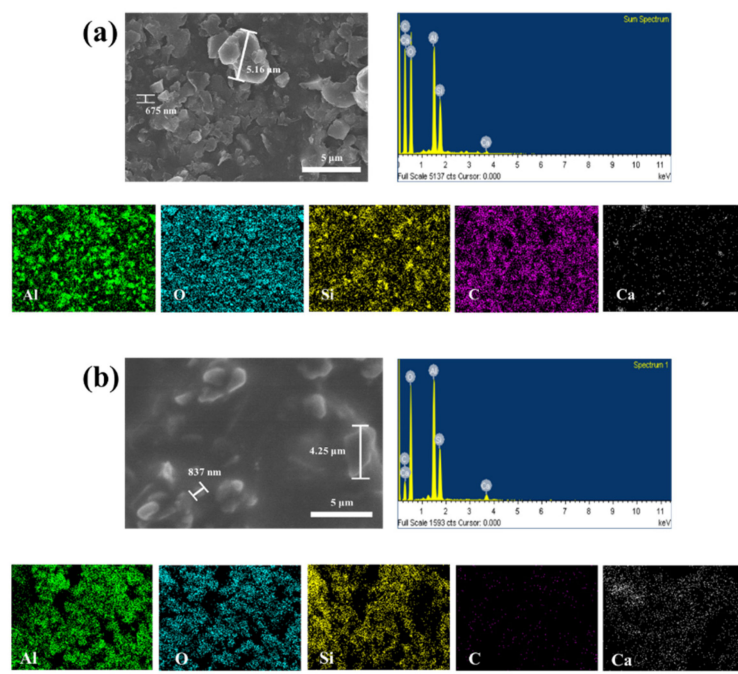


Figure 7. (a) FE-SEM image and EDAX spectrum of the ceramic particles at the green body, (b) FE-SEM image and EDAX spectrum of the ceramic particles sintered at 1300 °C after C-step debinding.

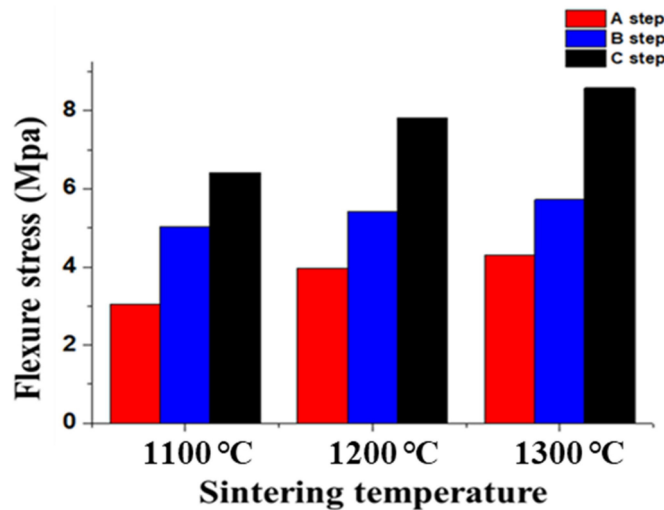


Figure 8. Bending strength of ceramics sintered at different temperatures with A, B, and C debinding steps.

Figure 9 shows the complex lattice structure resulting from the debinding and sintering processes with optimized conditions for ceramic green bodies fabricated by the DLP 3D printing method. Accordingly, the possibility of fabricating structures with complex geometries by DLP 3D printing using the optimized debinding and sintering processes was presented. Finally, DLP 3D ceramic printing technology has high precision and excellent thermal stability of ceramics. Therefore, high-performance products such as high-efficiency

microturbine rotors and high-temperature microreactors are currently manufactured in real industry. Microturbine rotors and high-temperature micro-reactors require excellent thermal stability and mechanical properties. In order to obtain these characteristics, we require the development of optimization of ceramic slurry between ceramic powder and resin. Recently, the developed ceramic slurries have consisted of high purity ceramic powder of about 99%. Moreover, the ceramic slurries have been developed by optimizing the ceramic concentration in the slurry to increase the photo-curing efficiency.

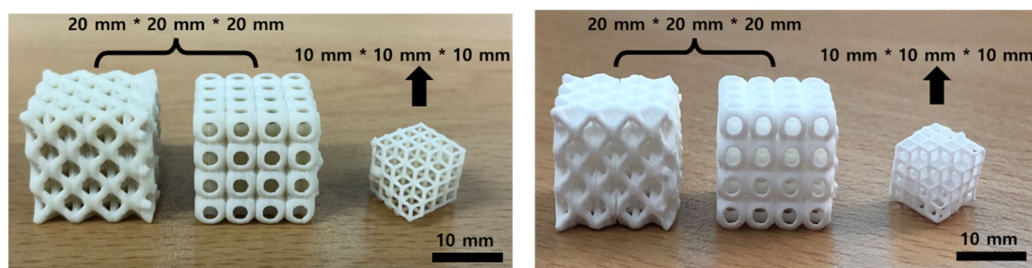


Figure 9. Ceramic with a lattice structure using DLP 3D printing. (a) Green bodies, (b) sintered bodies.

4. Conclusions

This study confirmed that the density of a ceramic body sintered at 1300 °C with a 6 h holding time (C step) for debinding was 1.36 g/cm³ and the linear shrinkage rate was 22.1/21.6/28.5% for the x, y, and z axes, respectively. The bending strength was 8.58 MPa. Through FTIR, XRD, and EDAX analyses, the presence of a binder inside the sintered body, as well as the phase composition, were confirmed. The SEM images showed that the pore size was reduced and the densification gradually increased as the debinding holding time and sintering temperature increased. The ceramic sample fabricated in this study had lower strength than that of the Al₂O₃ ceramic fabricated by the existing DLP 3D printing method and sintered at 1300 °C. This might be because of the ceramic content in the slurry. When the ceramic content was high, the amount of binder released after debinding was reduced, so that the number and size of pores were reduced. Therefore, decreased mechanical properties were caused by increased porosity. In this study, the changes in mechanical properties were confirmed according to the holding time of debinding and sintering temperature when manufacturing a ceramic sintered body using the DLP 3D printing method, and the possibility of manufacturing a complex geometry was presented.

Author Contributions: Conceptualization, J.-H.S.; methodology, B.-K.K.; writing—original draft preparation J.-H.S.; writing—review and editing, D.-S.K. and M.J. All authors have read and agreed to the published version of the manuscript.

Funding: This research was supported by Basic Science Research Program through the National 245 Research Foundation of Korea (NRF) funded by the Ministry of Education 246 (No. 2018R1A6A1A030 26005). This research was supported by the research fund of Hanbat National University.

Data Availability Statement: Not applicable.

Conflicts of Interest: The authors declare no conflict of interest.

References

- Chen, Z.; Li, Z.; Li, J.; Liu, C.; Lao, C.; Fu, Y.; Liu, C.; Li, Y.; Wang, P.; He, Y. 3D printing of ceramics: A review. *J. Eur. Ceram. Soc.* **2019**, *39*, 661–687. [[CrossRef](#)]
- He, R.; Liu, W.; Wu, Z.; An, D.; Huang, M.; Wu, H.; Jiang, Q.; Ji, X.; Wu, S.; Xie, Z. Fabrication of complex-shaped zirconia ceramic parts via a DLP-stereolithography-based 3D printing method. *Ceram. Int.* **2018**, *44*, 3412–3416. [[CrossRef](#)]
- Varghese, G.; Moral, M.; Castro-García, M.; López-López, J.J.; Marín-Rueda, J.R.; Yagüe-Alcaraz, V.; Hernández-Afonso, L.; Carlos Ruiz-Morales, J.; Canales-Vázquez, J. Fabrication and characterisation of ceramics via low-cost DLP 3D printing. *Boletín Soc. Española Cerámica Vidr.* **2018**, *57*, 9–18. [[CrossRef](#)]

4. Li, S.; Duan, W.; Zhao, T.; Han, W.; Wang, L.; Dou, R.; Wang, G. The fabrication of SiBCN ceramic components from preceramic polymers by digital light processing (DLP) 3D printing technology. *J. Eur. Ceram. Soc.* **2018**, *38*, 4597–4603. [[CrossRef](#)]
5. Zhang, C.; Luo, Z.; Liu, C.; Zhu, J.; Cao, J.; Yuan, J.; Wang, P.; Liu, C.; Lao, C.; Chen, Z. Dimensional retention of photocured ceramic units during 3D printing and sintering processes. *Ceram. Int.* **2021**, *47*, 11097–11108. [[CrossRef](#)]
6. Zheng, T.; Wang, W.; Sun, J.; Liu, J.; Bai, J. Development and evaluation of Al₂O₃-ZrO₂ composite processed by digital light 3D printing. *Ceram. Int.* **2020**, *46*, 8682–8688. [[CrossRef](#)]
7. Fan, J.; Xu, X.; Niu, S.; Zhou, Y.; Li, X.; Guo, Y.; Luo, Y. Anisotropy management on microstructure and mechanical property in 3D printing of silica-based ceramic cores. *J. Eur. Ceram. Soc.* **2022**, *42*, 4388–4395. [[CrossRef](#)]
8. Mamatha, S.; Biswas, P.; Ramavath, P.; Das, D.; Johnson, R. Effect of parameters on 3D printing of alumina ceramics and evaluation of properties of sintered parts. *J. Asian Ceram. Soc.* **2021**, *9*, 858–864. [[CrossRef](#)]
9. Chen, R.; Duan, W.; Wang, G.; Liu, B.; Zhao, Y.; Li, S. Preparation of broadband transparent Si₃N₄-SiO₂ ceramics by digital light processing (DLP) 3D printing technology. *J. Eur. Ceram. Soc.* **2021**, *41*, 5495–5504. [[CrossRef](#)]
10. Kovacev, N.; Li, S.; Essa, K. Effect of the preparation techniques of photopolymerizable ceramic slurry and printing parameters on the accuracy of 3D printed lattice structures. *J. Eur. Ceram. Soc.* **2021**, *41*, 7734–7743. [[CrossRef](#)]
11. Truxova, V.; Safka, J.; Seidl, M.; Kovalenko, I.; Volesky, L.; Ackermann, M. Ceramic 3D printing: Comparison of SLA and DLP technologies. *MM Sci. J.* **2020**, *3905–3911*. [[CrossRef](#)]
12. Wang, K.; Qiu, M.; Jiao, C.; Gu, J.; Xie, D.; Wang, C.; Tang, X.; Wei, Z.; Shen, L. Study on defect-free debinding green body of ceramic formed by DLP technology. *Ceram. Int.* **2020**, *46*, 2438–2446. [[CrossRef](#)]
13. Shuai, X.; Zeng, Y.; Li, P.; Chen, J. Fabrication of fine and complex lattice structure Al₂O₃ ceramic by digital light processing 3D printing technology. *J. Mater. Sci.* **2020**, *55*, 6771–6782. [[CrossRef](#)]
14. Li, H.; Liu, Y.; Liu, Y.; Zeng, Q.; Hu, K.; Lu, Z.; Liang, J.; Li, J. Influence of debinding holding time on mechanical properties of 3D-printed alumina ceramic cores. *Ceram. Int.* **2021**, *47*, 4884–4894. [[CrossRef](#)]
15. Sun, L.; Dong, P.; Zeng, Y.; Chen, J. Fabrication of hollow lattice alumina ceramic with good mechanical properties by Digital Light Processing 3D printing technology. *Ceram. Int.* **2021**, *47*, 26519–26527. [[CrossRef](#)]
16. Zhou, M.; Liu, W.; Wu, H.; Song, X.; Chen, Y.; Cheng, L.; He, F.; Chen, S.; Wu, S. Preparation of a defect-free alumina cutting tool via additive manufacturing based on stereolithography—Optimization of the drying and debinding processes. *Ceram. Int.* **2016**, *42*, 11598–11602. [[CrossRef](#)]
17. Kang, K.H.; Jeon, S.H.; Hyun, M.H.; Lee, D.K. Synthesis of Cubic and Rod Shapes CaCO₃ by Hydrothermal Method. *J. Korea Acad. Ind.* **2016**, *17*, 255–261.
18. Shamsudin, R.; Abdul Azam, F.A.; Abdul Hamid, M.A.; Ismail, H. Bioactivity and Cell Compatibility of β -Wollastonite Derived from Rice Husk Ash and Limestone. *Materials* **2017**, *10*, 1188. [[CrossRef](#)]
19. Anbalagan, G.; Prabakaran, A.; Gunasekaran, S. Spectroscopic characterization of Indian standard sand. *J. Appl. Spectrosc.* **2010**, *77*, 86–94. [[CrossRef](#)]
20. Mohammed, A.A.; Khodair, Z.T.; Khadom, A.A. Preparation and investigation of the structural properties of α -Al₂O₃ nanoparticles using the sol-gel method. *Chem. Data Collect.* **2020**, *29*, 100531. [[CrossRef](#)]
21. Zhang, C.; Xu, Z.; Hu, Y.; He, J.; Tian, M.; Zhou, J.; Zhou, Q.; Chen, S.; Chen, D.; Chen, P.; et al. Novel insights into the hydroxylation behaviors of α -quartz (101) surface and its effects on the adsorption of sodium oleate. *Minerals* **2019**, *9*, 450. [[CrossRef](#)]
22. Redemeyer, H.; Launspach, M. Detection of interaction between biomineralling proteins and calcium carbonate microcrystals. *Beilstein J. Nanotechnol.* **2011**, *2*, 222–227. [[CrossRef](#)] [[PubMed](#)]
23. Núñez-Rodríguez, L.A.; Encinas-Romero, M.A.; Gómez-Álvarez, A.; Valenzuela-García, J.L.; Tiburcio-Munive, G.C. Evaluation of Bioactive Properties of α and β Wollastonite Bioceramics Soaked in a Simulated Body Fluid. *J. Biomater. Nanobiotechnology* **2018**, *9*, 263–276. [[CrossRef](#)]
24. Li, H.; Liu, Y.; Liu, Y.; Zeng, Q.; Hu, K.; Lu, Z.; Liang, J. Effect of sintering temperature in argon atmosphere on microstructure and properties of 3D printed alumina ceramic cores. *J. Adv. Ceram.* **2020**, *9*, 220–231. [[CrossRef](#)]
25. Grigoriev, S.N.; Fedorov, S.V.; Hamdy, K. Materials, properties, manufacturing methods and cutting performance of innovative ceramic cutting tools—A review. *Manuf. Rev.* **2019**, *6*, 19. [[CrossRef](#)]
26. Yang, J.F.; Ohji, T.; Kanszki, S.; Díaz, A.; Hampshire, S. Microstructure and mechanical properties of silicon nitride ceramics with controlled porosity. *J. Am. Ceram. Soc.* **2002**, *85*, 1512–1516. [[CrossRef](#)]
27. Santoliquido, O.; Camerota, F.; Ortona, A. The influence of topology on DLP 3D printing, debinding and sintering of ceramic periodic architectures designed to replace bulky components. *Open Ceram.* **2021**, *5*, 100059. [[CrossRef](#)]